Supporting Information for: Imaging Carrier Inhomogeneities in Ambipolar Tellurene Field Effect Transistors

Samuel Berweger,[*,†,‡] Gang Qiu,[¶,§] Yixiu Wang,[‖] Benjamin Pollard,[‡] Kristen L. Genter,[†,⊥] Robert Tyrrell-Ead,[†] T. Mitch Wallis,[†] Wenzhuo Wu,[‖,§] Peide D. Ye,[¶,§] and Pavel Kabos[†]

†*Applied Physics Division, National Institute of Standards and Technology, Boulder, CO*

‡*Department of Physics, University of Colorado, Boulder, CO*

¶*School of Electrical and Computer Engineering, Purdue University, West Lafayette, IN*

§*Birck Nanotechnology Center, Purdue University, West Lafayette, IN*

‖*School of Industrial Engineering, Purdue University, West Lafayette, IN*

⊥*Department of Mechanical Engineering, University of Colorado, Boulder, CO*

E-mail: samuel.berweger@nist.gov

Here we provide the full data sets for the devices shown in the manuscript, as well as an additional thin device.

Shown in Fig. S1 is the full data set for the device shown in Figs. 2 and 3 of the manuscript. This device is fabricated on 90 nm of SiO_2 with a 10 nm conformal overcoat of alumina (Al_2O_3) deposited to prevent electrical discharge from the tip to the device. For this particular device the global carrier equivalence point is observed to occur at $V_{BG} = 20$ V. Shown in Fig. S2 is the full data set for a device fabricated under identical conditions as the one in Fig. S1 with a thickness of ∼8 nm. The device carrier equivalence point is measured

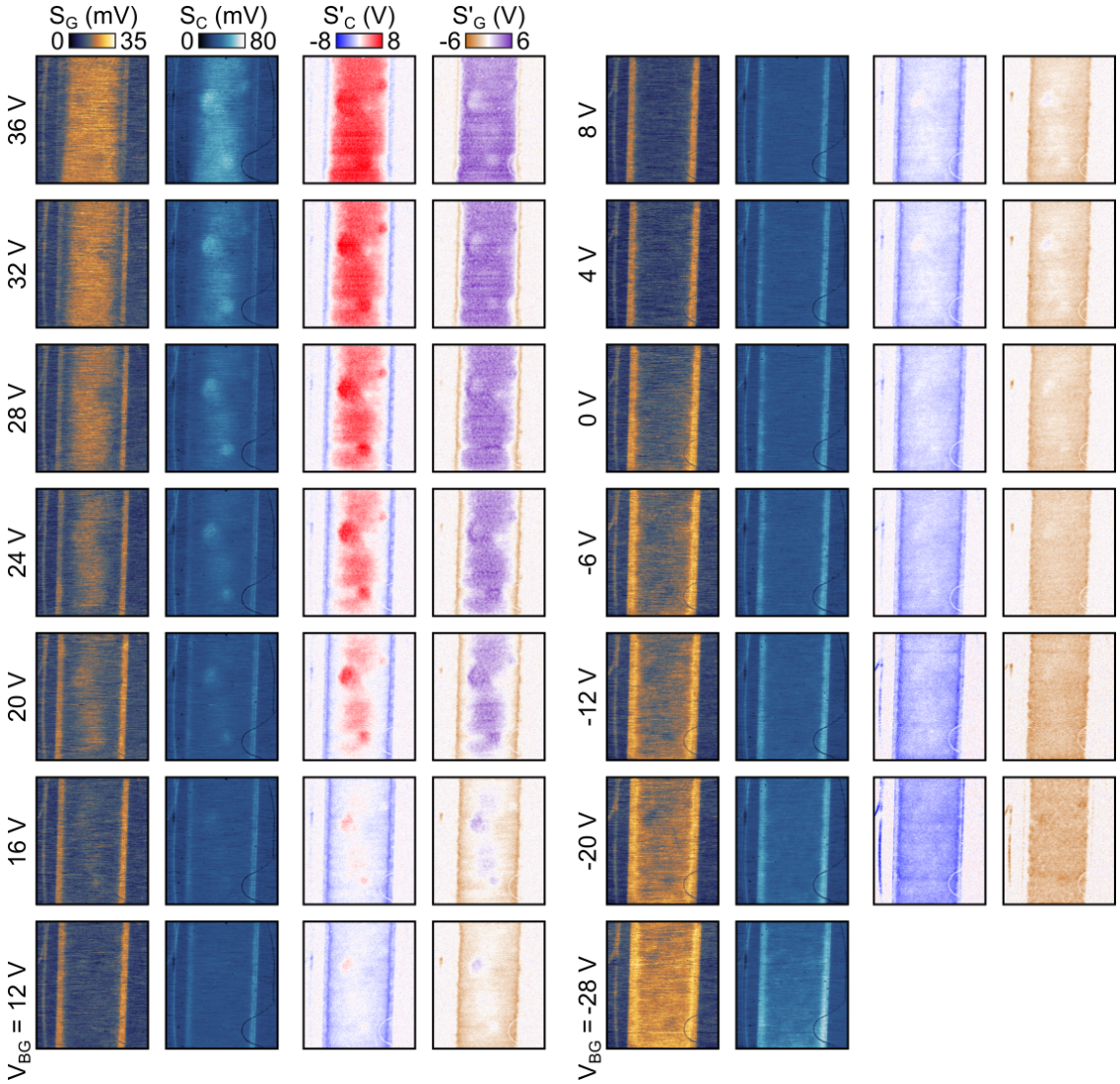

Figure S1: Full data set to device shown in Figs. 2 and 3 of the manuscript.

to be at $V_{BG} = 0$ V. With both of these devices Te filaments are seen next to as well as on top of the devices, though the electrical impact of these appears to be weak.

Shown in Fig. S3a) is the complete data set for the device shown in Fig. 4 of the manuscript. This device was fabricated on 300 nm oxide with a 10 nm conformal overcoat of hafnia (HfO_2). Due to the thicker oxide, larger backgate voltages are required for effective gating, the device can readily sustain biases of up to $V_{BG} = \pm 100$ V, and the global carrier equivalence point is seen to occur at $V_{BG} = 60$ V. Importantly, based on the AFM topography we infer that the filament is embedded beneath the device, significantly affecting

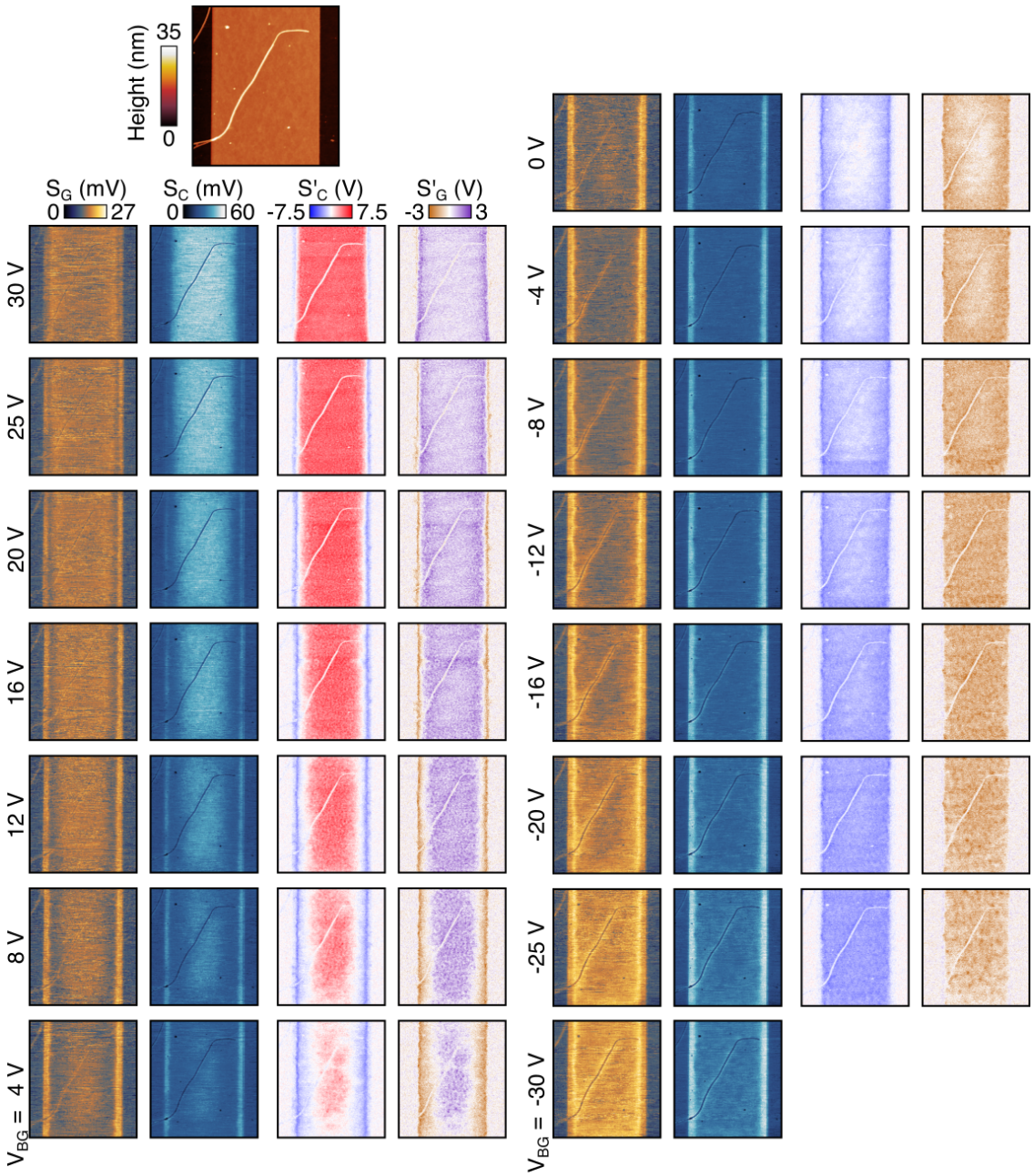

Figure S2: Full data set for an additional device. This device is similar to the one shown in Figs. 2 and 3 of the manuscript with similar thickness and overall size. For this particular device the device carrier equivalence point is measured to be at $V_{BG} = 0$ V.

the spatial carrier distribution. For this device only S'_C and S'_G were measured.

Shown in Fig. S3b) and c) are the V_{BG}-dependent values of S'_C and S'_G. We see that the zero-crossing of interest, representing the local carrier equivalence point is the same for both data channels, as expected. In order to optimally extract the zero-crossing and

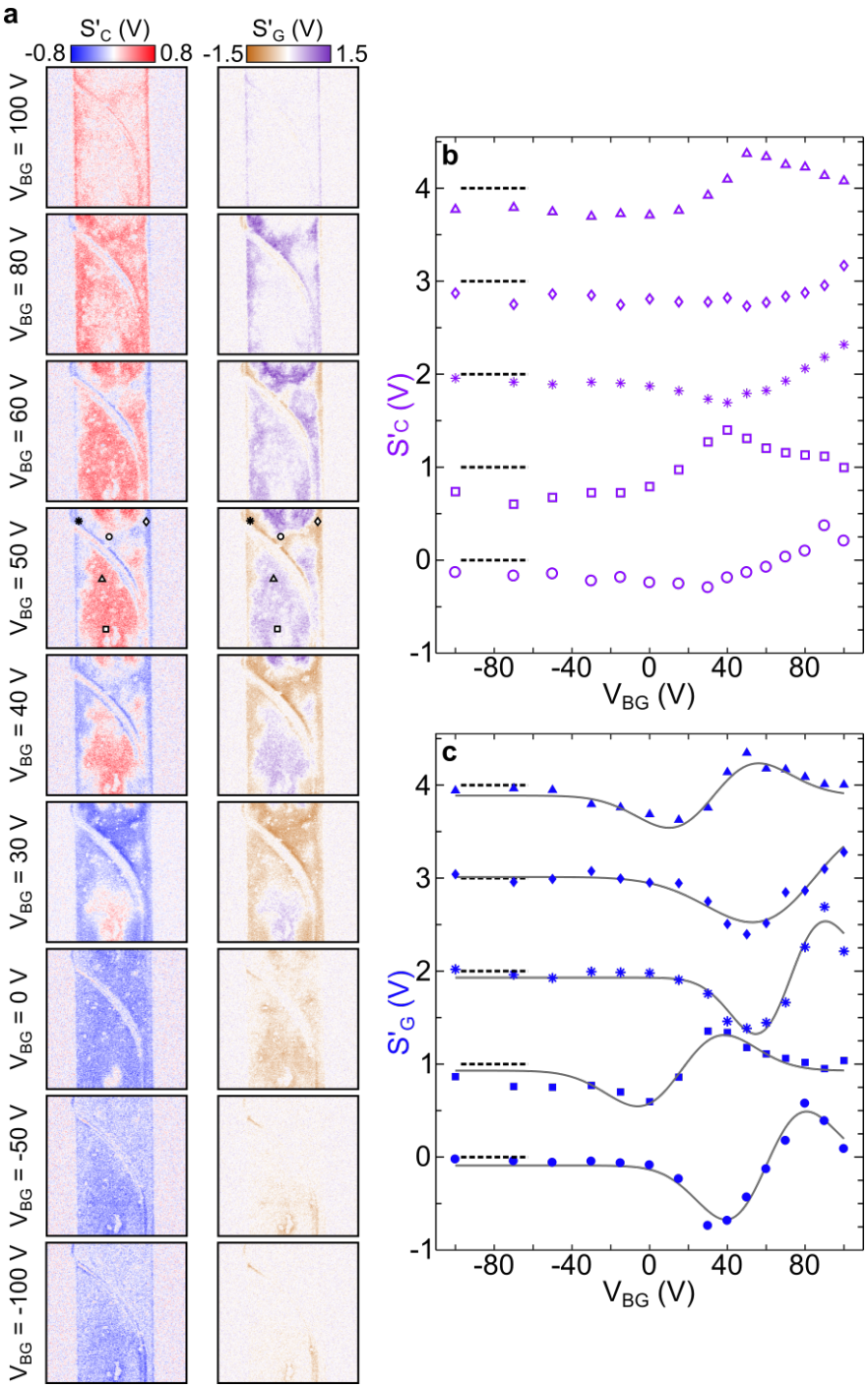

Figure S3: Full data set for the device shown in Fig. 4 of the manuscript.

enable extrapolation to values outside of the measured range, we observe that an excellent

phenomenological fit to S'_G can be obtained of the functional form:

$$\frac{dG}{dV}(V_{BG}) = A_o + A(V_o - V_{BG})e^{-\frac{(V_o - V_{BG})^2}{2\sigma^2}}. \quad \text{(S1)}$$

with the fit to each curve shown by the gray lines in Fig. S3c). The carrier equivalence point voltages shown in Fig. 4d) of the manuscript are given by the values of V_o extracted at each spatial pixel by fitting Eq. S1.

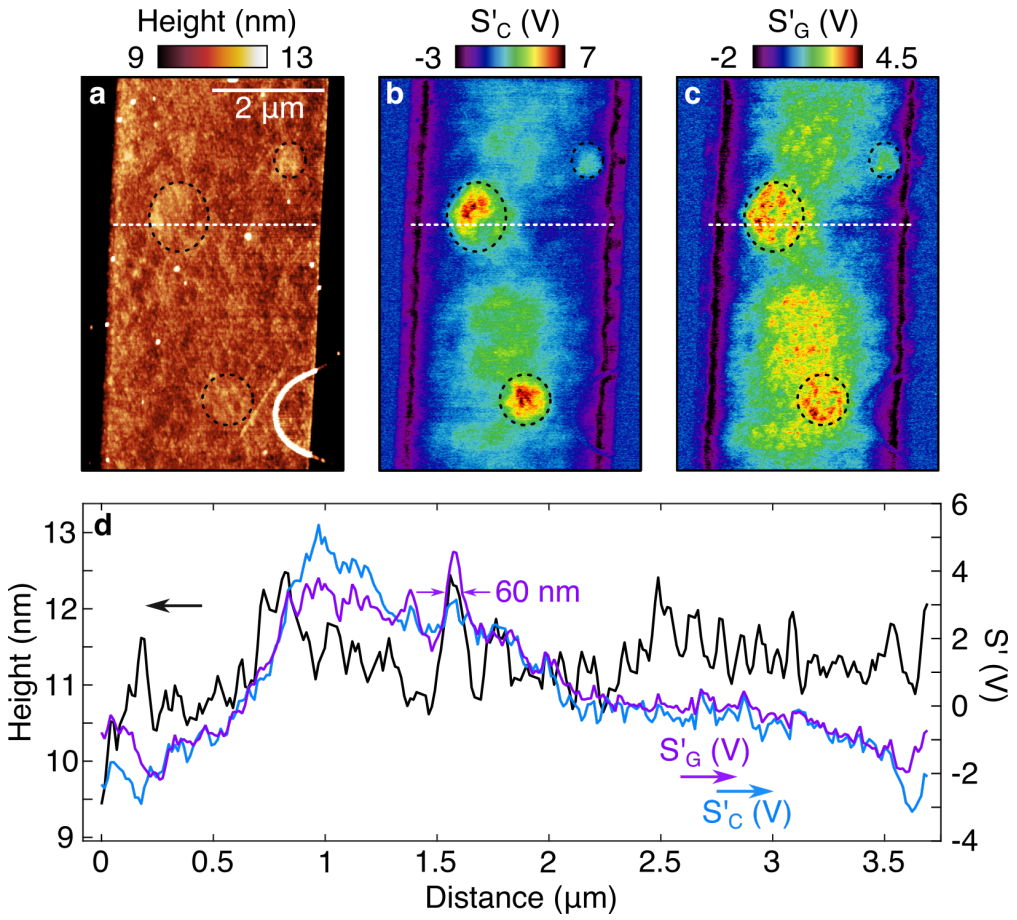

Figure S4: High-resolution AFM topography (a) and the corresponding S'_C (b) and S'_G (c) images showing small features within the Te crystal. (d) line scan taken along the white dashed line.

Lastly, we show a high resolution image of a device. Shown in Fig. S4 are the high resolution (∼13 nm pixel size) topography (a) and corresponding S'_C (b) and S'_G (c) images of the device shown in Fig. S1 and Figs. 2 and 3 with $V_{BG} = 16$ V (as this scan is not part

of a sequence, some hysteresis is expected relative to the scans in Figures 3 and S1). The colorbars for all images have been scaled to optimize the visibility of small features within the tellurene crystal. In the topography we see striations that align along the length of the crystal while in the microwave near-field image we see signal variations on sub-μm length scales. A line cut (d) taken along the white dashed line reveals that although S'_C and S'_G agree well and most features are reproduced in both channels, they correlate only weakly with the topography. In particular, we see that some of the topographic variations correlate with increases in the microwave near-field signal, though many do not. We note that we cannot discern changes in height due to local variations in thickness in the ALD overcoat from those due to structural or morphological variations in the underlying Te device. However, several regions enclosed by black dashed lines appear thicker in the topography and exhibit an overall stronger microwave near-field signal, suggesting that these signal variations may arise due to the probing of a thicker Te region underneath. With topographic variations of a few nm, the expected effects of topographic artifacts in these measurements are expected to be negligible, particularly for differential measurements, as further confirmed by the weak correlation between topography and microwave near-field signal here.

Lastly we use the full-width at half-maximum of a well-resolved feature in S'_G to provide an estimate of the achieved spatial resolution of 60 nm as indicated. We note that we observe features in the scan that indicate a higher achieved spatial resolution, and it is thus possible that the observed 60 nm width is not in fact limited by the spatial resolution but the size of the resolved feature.